

## Chapter 2

# Calculating the Structural Preference of High Symmetry Clusters for $\text{Pd}_N$ , $\text{Au}_N$ , and $(\text{PdAu})_N$

## 2.1 Introduction

Computational modelling plays an important role in understanding the properties of nanoclusters, as it allows the prediction of structures for the lowest energy isomer (i.e. the global minimum, GM) [1], as well as providing information on preferential cluster geometries [2], or local minima, and further details such as metal segregation in bimetallic systems [3]. In this chapter the relative energetics will be discussed for different high-symmetry structures composed of Pd, Au, or a combination of the two. Clusters have been created using mathematical constructs, and then energetically minimised. Stability trends are identified for different compositions and geometries, in order to compare our results with experimental observations.

A large amount of computational research work has been done previously on both homogeneous and heterogeneous clusters; recent comprehensive reviews have been carried out by Baletto et al. [4] and Ferrando et al. [3] respectively, and we highlight some of the key publications below.

### 2.1.1 $\text{Pd}_N$ Clusters

The energetics of small Pd nanoparticles have been thoroughly investigated by several computational groups using first-principle techniques [2, 5–10]. Besides their catalytic properties, work on these clusters is interesting as their lowest-lying isomer may have nonzero spin [11], thus being magnetic. At large sizes *ab initio* calculations are rare due to their computational expense: DFT calculations by Nava et al. found an early preference for bulk-like structures when the number of atoms  $N > 100$ , with a larger binding energy ( $E_b$ ) for FCC geometries than icosahedra (Ih) or Ino-decahedra (I-Dh) [5]—however at “magic numbers” Ih and cuboctahedra (CO) remain very energetically competitive; a result confirmed by Guirado-López et al. [9]. Work by Baletto and Ferrando using the RGL potential [12, 13] on large

$\text{Pd}_N$  clusters ( $N < 5,000$ ) reviewed relative geometric stabilities over a wide range of sizes, showing a preferential trend of Ih for low nuclearities, FCC for large nuclearities and M-Dh in between, with interval windows greater than observed in a similar study of  $\text{Au}_N$  clusters [2].

In experiments, José-Yacamán et al. observed thiol-passivated Pd nanoparticles by TEM, witnessing structures ranging from crystalline (FCC) to high-symmetry (Ih); very large Ih were also observed, their presence associated with kinetic trapping effects, and these results were backed up with theoretical images [14]. A review of other recent work on Pd nanoclusters by José-Yacamán and co-workers reaffirms the presence of a variety of structures, and also mentions the influence the substrate may have upon structural growth [15]. Size-selected  $\text{Pd}_N$  clusters were studied by Pearmain [16] using scanning transmission electron microscopy (STEM). A mixture of Ih, I-Dh and FCC structures were identified for  $N = 887$ , as well as structural changes for larger nuclearities used in catalytic processes.

### 2.1.2 $\text{Au}_N$ Clusters

Small  $\text{Au}_N$  clusters ( $N \leq 10$ ) have been thoroughly investigated using *ab initio* techniques, showing a preference for planar geometries [17–19]. DFT calculations and IR photodepletion experiments have shown that  $\text{Au}_{20}$  is a tetrahedron [20, 21], with FCC packing; for other sizes low-symmetry structures are known to be energetically competitive [22]. For larger clusters *ab initio* calculations are less feasible: as previously mentioned Baletto and Ferrando carried out calculations on high-symmetry structures using the RGL potential, where a preferential structural interval for Ih was identified for  $0 < N \lesssim 50$ , followed by a M-Dh interval of similar size ( $50 \lesssim N \lesssim 100$ ) [2]. After this crystalline structures were prominent, and similar results were found by various other groups using other semi-empirical potentials [23, 24].

Experimental studies of  $\text{Au}_N$  clusters are difficult as they are often passivated after formation, and it is difficult to know what effect the support agents have [25]. Recently Häkkinen, Akola and co-workers performed geometry calculations for thiolate-supported of  $\text{Au}_{25}$ ,  $\text{Au}_{38}$ ,  $\text{Au}_{102}$ , and  $\text{Au}_{144}$  systems, as well as other phosphine-halide stabilised Au nanoparticles in the same size-range using DFT and matching their results to experimental X-ray diffraction patterns [26–31]. The calculations indicate that small ( $\leq 2\text{nm}$ ) passivated Au nanoparticles can be viewed as electronically stable superatoms with interesting atomic rearrangements at the interface between the metallic core and ligand-shell.

Experimentally, Wang et al. looked at characterising the thiolate-supported  $\text{Au}_{38}$  clusters using STEM, however the emphasis of this work was on atom counting as the low-symmetry of small clusters makes identifying motifs difficult [32]. Li, Palmer, Johnston and co-workers [33, 34] identified  $\text{Au}_{309}$  cluster geometries by comparing experimental HAADF-STEM images with image simulations (based on low energy structures found using the semi-empirical Gupta potential), and found

a number of competing structures; Ih, I-Dh and crystalline (FCC-like) geometries were all observed. STEM characterisation of  $\text{Au}_{887}$  is of current interest to this group of collaborators, for comparison with the previously mentioned  $\text{Pd}_{887}$  [35]. Stellated  $\text{Au}_N$  structures have been reported experimentally by the group of José-Yacamán [36], and  $\text{Au}_{887}$  is suspected to favour similar increased faceting.

### 2.1.3 $(\text{PdAu})_N$ Clusters

Empirical calculations for small  $(\text{PdAu})_N$  clusters have been conducted by the Johnston group using the Gupta Potential coupled with a genetic algorithm (GA) [37] for  $N < 50$  [38], and also specifically  $N = 34$  and  $38$  [39]. In both these works various potential parameter sets were tested, with parameters first derived by Cleri and Rosato [12] proving to favour  $\text{Pd}_{\text{core}}\text{Au}_{\text{shell}}$  segregation, whilst more recent parameters derived from *ab initio* calculations indicated a more mixed configuration; higher level calculations were unable to offer any more conclusive opinions on the matter. These findings highlight the sensitivity of structural configurations on the parameter sets used, especially at small sizes [39].

Calculations for larger clusters using the embedded-atom model (EAM) showed preference for  $\text{Pd}_{\text{core}}\text{Au}_{\text{shell}}$  segregation [40], which has been backed up by classical molecular dynamics (MD) calculations indicating core/shell inversion from  $\text{Au}_{\text{core}}\text{Pd}_{\text{shell}}$  to  $\text{Pd}_{\text{core}}\text{Au}_{\text{shell}}$  above 500 K [41]; the lower surface energy ( $E_{\text{surf}}$ ) of gold (Au:  $96.8 \text{ meV } \text{\AA}^{-2}$ , Pd:  $131 \text{ meV } \text{\AA}^{-2}$  [42]) is thought to be the driving force behind this configuration. Experimental work conducted in the same article reports the successful synthesis of  $\text{Au}_{\text{core}}\text{Pd}_{\text{shell}}$ ,  $\text{Pd}_{\text{core}}\text{Au}_{\text{shell}}$  and mixed PdAu nanoparticles [41], showing thermodynamic driving forces may be restricted by kinetic trapping depending on the synthetic method. In larger clusters, Ferrer et al. have reported the experimental formation of tri-layered Au/Pd nanoparticles [43].

## 2.2 Methodology

### 2.2.1 High Symmetry Structures

It has been shown that three common high-symmetry 12-vertex geometries, namely the Ih, I-Dh and CO, can be arranged from the same “magic number” nuclearities given by the third-order polynomial [44]:

$$N(k) = \frac{1}{3}[10k^3 + 15k^2 + 11k + 3] \quad (2.1)$$

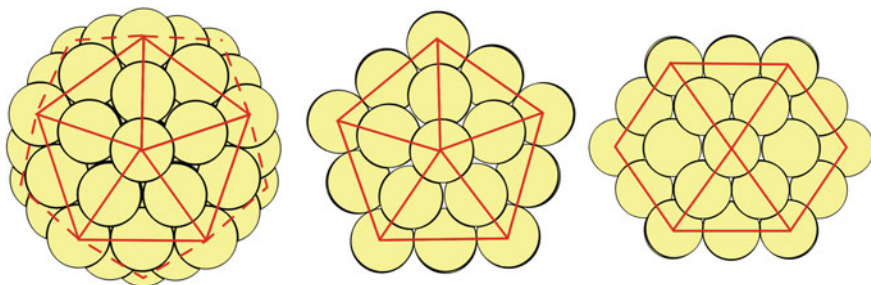


**Fig. 2.1** High symmetry structures with matching magic number nuclearities; illustrated for  $k = 2$  ( $N = 55$ ). From left to right: Ih, I-Dh and CO. Predominate faces are outlined in *solid red lines*, whilst background faces are marked with *dashed red lines*. Reproduced from [46] by permission of The Royal Society of Chemistry

where  $k$  is the number of shells in the structure—the first few values of  $N$  (i.e. “magic numbers”) in this sequence are 13, 55, 147 and 309. Increases in  $k$  lead to a larger value of  $N$  but a lower proportion of surface atoms, which can be approximated as  $N^{\frac{2}{3}}$ .

Each of these identified structures (Ih, I-Dh and CO) have distinct atomic arrangements with respect to each other, leading to differing attributes (Fig. 2.1, left). The Ih consists of 20 (111) faces, making it the most spherical of the three structures. This arrangement minimises the surface area to volume ratio, whilst maximising nearest neighbours contact, at the expense of high strain energy. The Ih geometry is most common for small clusters, where the energetic cost of having large surfaces is too great unless exceptional electronic configurations exist [45]. For larger clusters the minimisation of internal strain energy is more important. The CO is a fragment of an FCC crystal, with 8 (111) faces and 6 (100 faces); strain energy is at its lowest due to the bulk crystal nature, and maintains a reasonable number of nearest-neighbour contacts (Fig. 2.1, right). The CO is most common for large clusters as we approach the bulk limit ( $N \rightarrow \infty$ ). The I-Dh occupies the transitional space between these two geometries, with its structure not containing the tight packing of the Ih structure nor the high surface area of the CO: it has 10 (111) faces and 5 (100) faces, and is most commonly seen for medium sized clusters (Fig. 2.1, centre).

A structure closely related to the I-Dh is the Marks-Decahedron (M-Dh). The M-Dh has an I-Dh structure at its centre, and on to the (100) faces (Fig. 2.2, centre) protruding facets grow, relieving some of the internal strain at the cost of greater surface area. One can calculate the magic numbers for M-Dh clusters as [2]:

$$\begin{aligned}
 N(m, n, r) = & \frac{1}{6} \{ 30r^3 - 135r^2 + 207r - 102 \\
 & + [5m^3 + (30r - 45)m^2 + (60(r^2 - 3r) + 136)m] \\
 & + n[15m^2 + (60r - 75)m + 3(10r^2 - 30r) + 66] \} - 1 \quad (2.2)
 \end{aligned}$$

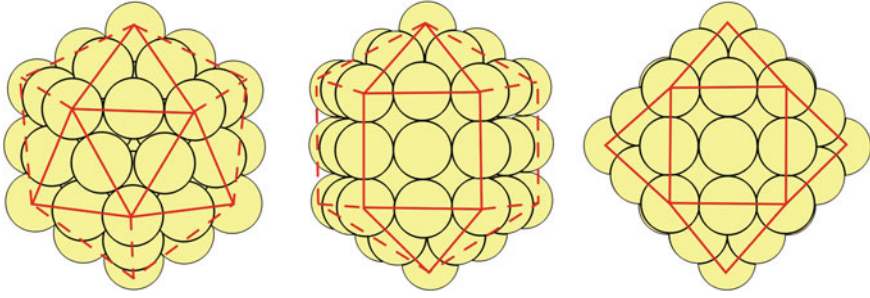


**Fig. 2.2** As for Fig. 2.1, with structures rotated by  $90^\circ$  around an ( $x$ -)axis positioned horizontally across the page. Reproduced from [46] by permission of The Royal Society of Chemistry

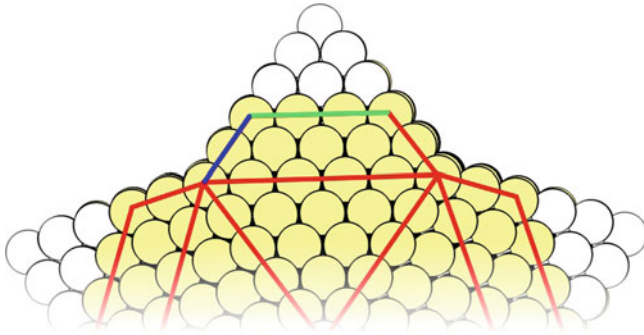


**Fig. 2.3** Diagram of the re-entrant faceting on the M-Dh structure; illustrated for  $(m, n, r) = (4, 4, 3)$ . Yellow spheres represent atoms in our model, whilst white spheres show the limit of re-entrant facets ( $r_{max} = 6$ ) on this size; this structure would be equivalent to setting  $(m, n, r) = (1, 1, 6)$ . Solid red lines define the faces on the  $(4, 4, 3)$  structure, with  $m$  (green) and  $r$  (blue) highlighted

where  $m$  and  $n$  are the lengths of the sides of the (100) facets perpendicular and parallel to the fivefold axis, respectively, and  $r$  is the depth of the Marks-type re-entrant facets. For  $r = 2$  and  $m = n$ , the magic numbers formed begin with the sequence  $N = 18, 75, 192$  and  $389$ . The maximum re-entrant depth ( $r_{max}$ ) is limited by the length of the side on the I-Dh core, such that  $r_{max} = k + 1$  (and when  $m = n$ ,  $r_{max} = m$ ) (Fig. 2.3).

Another high-symmetry structure often documented is the truncated octahedron (TO), a structure closely related to CO as both are fragments of the FCC crystal. The TO structure is created by the removal of the vertices from an octahedron to create a geometry with 6 (100) faces and 8 hexagonal (111) faces. We can define the number of atoms in the TO cluster [2]:

$$N(n_l, n_{cut}) = \frac{1}{3}(2n_l^3 + n_l) - 2n_{cut}^3 - 3n_{cut}^2 - n_{cut} \quad (2.3)$$

where  $n_l$  is the length of the edge of a complete octahedron and  $n_{cut}$  is the number of layers removed at each vertex. It should be noted here that the hexagonal (111) faces can have uneven sides, causing them to be irregular.

### 2.2.2 The Gupta Potential

It remains computationally exhaustive to perform *ab initio* calculations on large clusters ( $N > 100$ ), and so empirical potentials remain widely used. Empirical potentials are derived from the fitting of experimental data to an assumed functional form, with common examples including the Murrell-Mottram [47], Gupta [12], Sutton-Chen [48] and EAM [49]. When coupled with efficient search techniques (e.g. GAs [37]) highly effective theoretical tools are formed.

The Gupta potential, derived from Gupta's expression for the cohesive energy ( $E_{coh}$ ) of a bulk material [50], is based on the second moment approximation to tight-binding theory and is constructed from an attractive many-body ( $V^m$ ) term and a repulsive pair ( $V^r$ ) term, obtained by summing over all  $N$  atoms:

$$V_{clus} = \sum_{i=0}^N (V_i^r - V_i^m) \quad (2.4)$$

where

$$V_i^r(r_{ij}) = \sum_{j \neq i}^N A e^{-p(\frac{r_{ij}}{r_0} - 1)} \quad (2.5)$$

and

$$V_i^m(r_{ij}) = \left[ \sum_{j \neq i}^N \zeta^2 e^{-2q(\frac{r_{ij}}{r_0} - 1)} \right]^{\frac{1}{2}} \quad (2.6)$$

In these equations,  $r_{ij}$  represents the distance between atoms  $i$  and  $j$ ; and  $r_0$  is the nearest neighbour distance in the bulk (in Å). The Gupta potential parameters ( $A$ ,  $\zeta$ ,  $p$  and  $q$ ) are fitted to the bulk properties of each metal (i.e.  $E_{coh}$ , bulk modulus, the annihilation of the energy gradient at  $r_0$ , and in some cases the surface energy,  $E_{surf}$ ). After fitting to the bulk properties, one is left with only two independent parameters ( $p$  and  $q$ ) that determine the range of the repulsive and attractive terms, respectively. The parameter sets *I* and *II* used in the following work are taken from the work of Cleri and Rosato [12] and Baletto et al. [2], respectively, and are shown in Tables 2.1 and 2.2, and plotted in Appendix A. Parameter sets are not mixed, however arithmetic means are used for bimetallic Au-Pd interactions.

**Table 2.1** Gupta potential parameter sets *I* and *II* for Pd, taken from the work of Cleri and Rosato (*left*) and Baletto et al. (*right*), respectively [2, 12]

	Parameter Set <i>I</i> [12]	Parameter Set <i>II</i> [2]
A (eV)	0.1746	0.1715
$\zeta$ (eV)	1.718	1.702
p	10.867	11.00
q	3.742	3.79
$r_0$ (Å)	2.7485	2.7506

**Table 2.2** Gupta potential parameter sets *I* and *II* for Au, taken from the work of Cleri and Rosato (*left*) and Baletto et al. (*right*), respectively [2, 12]

	Parameter Set <i>I</i> [12]	Parameter set <i>II</i> [2]
A (eV)	0.2061	0.2197
$\zeta$ (eV)	1.790	1.855
p	10.229	10.53
q	4.036	4.30
$r_0$ (Å)	2.884	2.878

### 2.2.3 Long Range Cut-Off

The parameters used in reference [2] incorporate a long distance cut-off into the potential for atoms further than 2 neighbours distance away ( $>\sqrt{2}r$ ) [51]. The inter-atomic potential (Eq. 2.4) decays with increasing distance and introducing a cut-off speeds up the energy calculations for large clusters.

A 5th order polynomial was introduced, matching that of Baletto et al. [2]. For this, a polynomial replacement for the potential that matches the potential function at the cut-off start ( $C_s$ ), and is zero at the cut-off end ( $C_e$ ) is derived. The replacement is applied separately to each exponential component of the Gupta potential. Considering the term:

$$V_{ij}^r(r_{ij}) = Ae^{-p(\frac{r_{ij}}{r_0}-1)} \quad (2.7)$$

for  $C_s \leq r_{ij} \leq C_e$  we replace the above expression by the following polynomial  $p_1(r_{ij})$ :

$$V_{ij}^r(r_{ij}) = p_1(r_{ij}) = a_5(r_{ij} - C_e)^5 + a_4(r_{ij} - C_e)^4 + a_3(r_{ij} - C_e)^3 \quad (2.8)$$

where the coefficients  $a_5$ ,  $a_4$ ,  $a_3$  are chosen to match the function and its first and second derivatives for  $r_{ij} = C_s$ . For  $r = C_e$ ,  $p_1(r_{ij}) = 0$ . The form of the polynomial ensures that the conditions on the function and its first derivative are automatically matched for  $r_{ij} = C_e$ . In the same way, for the term:

**Table 2.3** Cut-offs and polynomial coefficients used for Au and Pd (to 4 significant figures) for parameter set *II*

	Parameter Set <i>II</i>	
	Pd	Au
$C_s$ (Å)	3.890	4.070
$C_e$ (Å)	4.764	4.984
$a_3$	$-5.732 \times 10^{-3}$	$-8.105 \times 10^{-3}$
$a_4$	$-8.477 \times 10^{-3}$	$-1.110 \times 10^{-2}$
$a_5$	$-5.723 \times 10^{-3}$	$-6.828 \times 10^{-3}$
$x_3$	-3.131	-2.232
$x_4$	-4.861	-3.258
$x_5$	-2.157	-1.383

$$\left[ V_{ij}^m(r_{ij}) \right]^{\frac{1}{2}} = \zeta e^{-q(\frac{r_{ij}}{r_0} - 1)} \quad (2.9)$$

the following polynomial,  $p_2(r_{ij})$ , is used:

$$\left[ V_{ij}^m(r_{ij}) \right]^{\frac{1}{2}} = p_2(r_{ij}) = x_5(r_{ij} - C_e)^5 + x_4(r_{ij} - C_e)^4 + x_3(r_{ij} - C_e)^3 \quad (2.10)$$

where the coefficients  $x_5$ ,  $x_4$ ,  $x_3$  are calculated to match the form of the Gupta function. The cut-off parameters used are given in Table 2.3, and included in the potential functions plotted in Appendix A.

### 2.2.4 Local Minimisation

The Limited-Memory Broyden-Fletcher-Goldfarb-Shanno algorithm (L-BFGS) algorithm [52], is a quasi-Newton method for finding the maxima and minima of a potential using a memory efficient gradient search. It computes the inverse Hessian ( $\frac{d^2x}{dy^2}$ ) matrices of a function, but unlike in the traditional Newtonian method which has memory requirements of  $N^2$  values, restricting the stored history to  $M$  steps results in a memory requirement of  $N \times M$  values. This results in approximation of the Hessians, slowing down the convergence, but increases processing speed dramatically and thus speeds up the calculations, especially for large clusters ( $N > 100$ ).

## 2.3 Energetic Analysis

In order to quantify our results, we must introduce several equations that allow us to compare cluster stability. Firstly we calculate the average binding energy per atom ( $E_b$ ) using:



$$E_b = \frac{E_{tot}}{N} \quad (2.11)$$

where  $E_{tot} = -V_{clus}$  is the total energy of the cluster. We can calculate relative stabilities ( $\Delta E_b$ ) of different geometries with identical nuclearities using:

$$\Delta E_b = E_{b_{Ih}} - E_{b_x} \quad (2.12)$$

where the binding energies of I-Dh or CO can be directly compared with Ih ( $E_{b_{Ih}}$ ) when substituted in for  $E_{b_x}$ . Positive values indicate reduced stability, and a negative value indicates increased stability, relative to the Ih. The ratio of excess energy ( $E_{exc}$ ) to the number of cluster surface atoms is given as [53, 54]:

$$\Delta = \frac{E_{exc}}{N^{\frac{2}{3}}} \quad (2.13)$$

and can be used as an indication of stability trends with size.  $E_{exc}$  is calculated as  $E_{tot} - NE_{coh}$ , where  $E_{coh}$  is the cohesive energy per atom in the bulk; thus  $E_{exc} \propto E_b$ .  $N^{\frac{2}{3}}$  is used as an approximation to the number of surface atoms. In bimetallic systems  $E_{exc}$  becomes  $E_{tot} - ME_{coh,a} - (N - M)E_{coh,b}$ , where  $M$  is the number of atoms of type  $a$ , and  $(N - M)$  is the number of atoms of type  $b$ . In general, we expect the following expression to hold for  $\Delta$  [53, 54]:

$$\Delta = \frac{aN + bN^{\frac{1}{3}} + cN^{\frac{2}{3}} + d}{N^{\frac{2}{3}}} \quad (2.14)$$

The numerator is still equivalent to  $E_{exc}$ , and in this expression the constant  $d$  comes from the strain created by the vertices of the cluster,  $cN^{\frac{1}{3}}$  represents strain from the edges,  $bN^{\frac{2}{3}}$  from surface facets and the volume term  $aN$  is due to internal strain.  $aN$  vanishes for FCC geometries as  $N \rightarrow \infty$ , as it is the bulk crystal structure, whilst strain is present for all other geometries. Minimisation of  $\Delta$  infers relative overall stability of a geometry.

## 2.4 Results and Discussion

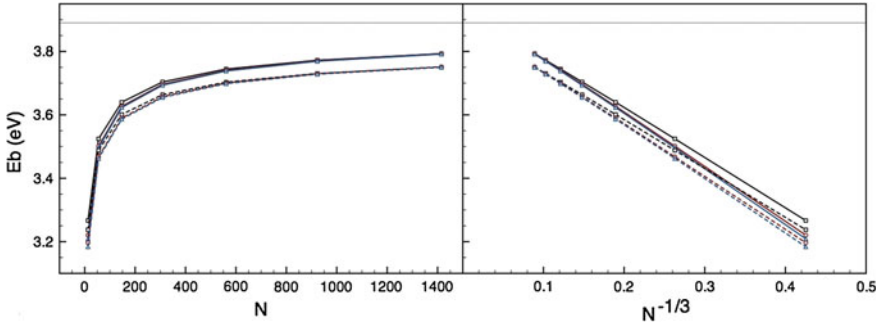
High-symmetry structures were systematically created using the mathematical constructs outlined above, before being energetically minimised using the parameters of either Cleri and Rosato [12] or Balleto et al. [2], henceforth referred to exclusively as parameter sets *I* and *II*, respectively.

### 2.4.1 $Pd_N$ Clusters

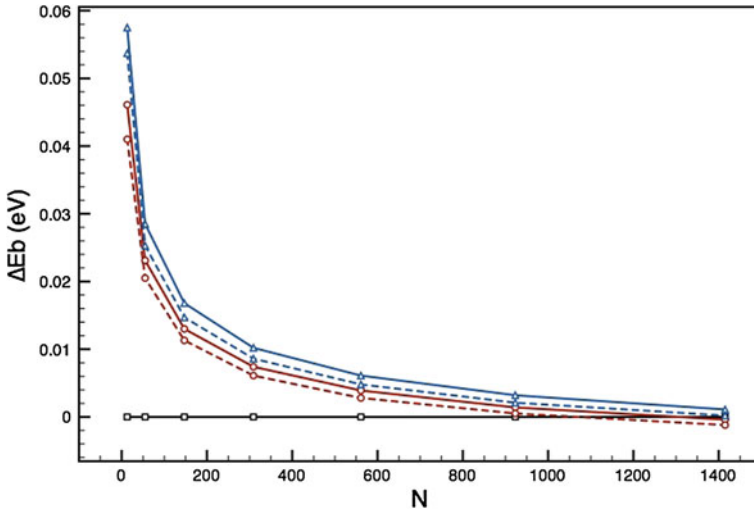
#### 12-Vertex Structures: Icosahedra, Ino-Decahedra and Cuboctahedra

Figure 2.4 plots  $E_b$  for Ih, I-Dh and CO structures, with increasing shell sizes  $k$ , against  $N$ , using the Pd parameters given in Table 2.1. For  $N < 100$ ,  $E_b$  rapidly increases, before levelling off as  $N > 500$ ; this trend is consistent for both parameter sets. Identification between the different structural motifs is energetically difficult, implying that they are all closely competitive in energy at this size. A spacing between trend lines is visible for the two parameter sets: parameter set *I* rises to a higher level than parameter set *II*, before flattening out asymptotically relative to  $E_{coh}$ . The difference in gradients between parameter sets *I* and *II* can be identified in the right of Fig. 2.4 where an approximation to the  $E_{coh}$  is achieved for  $N^{-\frac{1}{3}} \rightarrow 0$  when  $N^{-\frac{1}{3}}$  is plotted against  $E_b$ . Linear extrapolation to 0 for parameter set *I* gives a slightly over-exaggerated  $E_{coh}$  (3.92 eV) compared to the experimentally measured value (3.89 eV [52]), whilst parameter set *II* offers better agreement to this measurement (3.88 eV).

Figure 2.5 plots  $\Delta E_b$  in order to characterise the energetic preference of the Ih, I-Dh and CO structures in more detail. We can clearly see the close-packed Ih structure is the most stable for small sizes ( $N < 1,000$ ). For the parameter set *I*, the linear intercept between  $\Delta E_{bIh}$  and  $\Delta E_{bI-Dh}$  is at  $N = 1,306$ , whilst for parameter set *II* it is at  $N = 1,068$ .  $\Delta E_{bCO}$  remains positive throughout, and the intercept with  $\Delta E_{bIh}$  would be for a value of  $N > 1,500$ . We would expect the intercept of  $\Delta E_{bI-Dh}$  and  $\Delta E_{bCO}$  to be at large values of  $N$ , as discussed in our preamble.



**Fig. 2.4** Left: Plot of  $E_b$  for  $Pd_N$  structures against  $N$ . Solid lines represent the parameter set *I* of Cleri and Rosato [12], and dashed lines represent the parameter set *II* of Baletto et al. [2]. Right: Plot of  $E_b$  for  $Pd_N$  structures against  $N^{-\frac{1}{3}}$ . Ih (black squares), I-Dh (red circles) and CO (blue triangles) are shown in both plots;  $E_{coh}$  of 3.89 eV [52]) is displayed as a grey solid line



**Fig. 2.5** Plot of  $\Delta E_b$  for Ih (black squares), I-Dh (red circles) and CO (blue triangles)  $\text{Pd}_N$  structures against  $N$ . Solid lines represent the parameter set *I* of Cleri and Rosato [12], and dashed lines represent the parameter set *II* of Baletto et al. [2]

## FCC Structures

FCC structures with a variety of shapes were compared to the CO structure (Fig. 2.6a). For the FCC structures we find a spread  $1 \text{ eV} < \Delta < 2.2 \text{ eV}$ . It is noticeable that the structures that minimise  $\Delta$  for both the atom-centred and void-centred TO structures are closely competitive, with the adjoining lines difficult to distinguish. For both parameter sets *I* and *II* we find that the CO structure is uncompetitive with the lowest energy structures, which are TO, with  $\Delta(\text{TO})$  0.1 eV less than  $\Delta(\text{CO})$  for similar  $N$ : detailed analysis shows the more stable TO structures as those with reduced (100) surfaces compared to the hexagonal (111)-packed faces. In Fig. 2.6b and c, TO structures for  $\text{Pd}_{314}$  and  $\text{Pd}_{861}$  are presented: in these cases,  $n_l = 8$  and 11, respectively, and  $n_{cut} = 2$ .

Overall,  $\Delta$  is similar for the parameters sets *I* and *II* when  $N < 100$ , however for  $N > 500$  the minima of parameter set *I* are roughly 0.4 eV less than for parameter set *II*. Had we extended  $N$  further this gap would have increased, as the rate of change of the lowest values using parameter set *I* are considerably lower than that of parameter set *II*, though we would expect them to converge as  $N \rightarrow \infty$ .

## Marks-Decahedra

Systematic variation of the M-Dh structure enables a detailed analysis of the effect of the signature re-entrant facets, for which  $\Delta$  is plotted in Fig. 2.7. Trend lines are

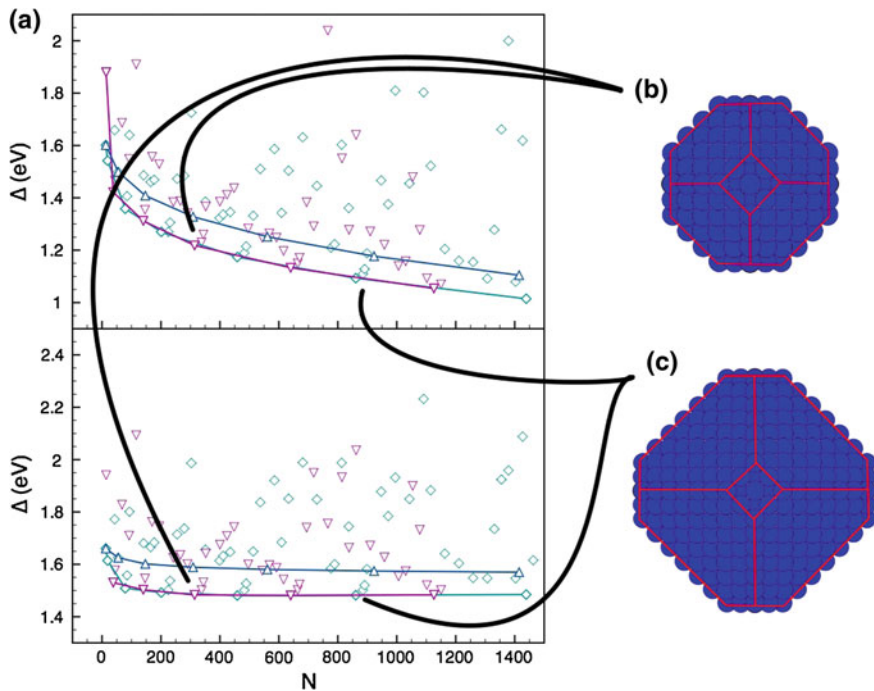


**Fig. 2.6** (a) *Top*: Plot of  $\Delta$  against  $N$  for various FCC  $\text{Pd}_N$  structures, where  $N < 1,500$ , for the parameter set *I* of Cleri and Rosato [12]. *Bottom*: As above, for the parameter set *II* of Baleto et al. [2]. TO structures with an atom at their centre (green diamonds) and with a void at their centre (purple downward triangles) are plotted against the CO structure (blue upward triangles) of increasing shell size  $k$ . Lines are plotted as a guide for the eye to the lowest values of  $\Delta$  for each structure type. Highlighted structures are (b)  $\text{Pd}_{314}$ , a void-centred TO, with faces highlighted by red lines and (c)  $\text{Pd}_{861}$ , an atom-centred TO, with faces highlighted with red lines. Adapted from [55] by permission of the PCCP Owner Societies

identified for differing values of  $r_{\max}$ , with their curved nature showing that the presence of truncated stellations is energetically favourable for both parameter sets *I* and *II* compared to the I-Dh structure, except at small sizes.

Parameter set *I* shows that the monolayer stellated structures ( $r = 2$ ) (truncated or not) are most energetically favourable for  $N < 600$ , where stellations are truncated to a single layer of atoms on the I-Dh core. For  $N > 600$  the ratio  $\frac{r}{r_{\max}}$  tends to a value of  $\sim 0.3$ , with multiple layers present on the truncated stellation. A progression in the trend lines occurs from sharp changes in  $\Delta$  to shallower, more spaced out  $\Delta$  values as  $N$  increases. The enlarged surface (100) sites on the I-Dh core (Fig. 2.2, centre) at large  $m$  and  $n$  mean even small re-entrant facets (e.g.  $r = 2$ ) make large overall contributions to the value of  $N$  and thus the spacing of data points. The same observations hold true for the parameter set *II*, with  $r = 2$  offering the lowest  $\Delta$  values relative to structures with fuller stellations at  $N < 300$ , and as  $N$  increases so  $r$  does also, e.g. for  $r_{\max} = 9$  a truncation of the full stellated edges so  $m = n = r = 5$

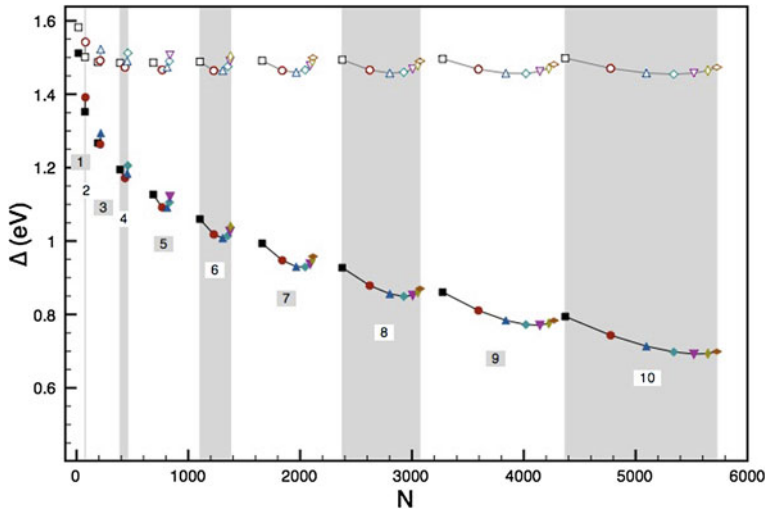


**Fig. 2.7** Plot of  $\Delta$  against  $N$  for  $\text{Pd}_N$  M-Dh of varying re-entrant facet sizes. Structures have been created such that  $r < 9$ , and  $m = n < 11$  where  $r = 2$  (black squares), 3 (red circles), 4 (blue upward triangles), 5 (green diamonds), 6 (purple downward triangles), 7 (yellow laterally-extended diamonds) and 8 (brown vertically-extended diamonds) are displayed. Parameter set *I*, of Cleri and Rosato [12], is plotted with open symbols and black trend lines, and parameter set *II*, of Baletto et al. [2], is plotted with closed symbols and grey trend lines. Trend lines illustrate the effect of reduced truncation of the stellated features from an I-Dh core ( $r = 1$ ) to fully stellated structures ( $m = 1$ ). Background colouring is added to highlight distinct trend lines.  $r_{\max}$  is given below each line. Reproduced from [55] by permission of the PCCP Owner Societies

is preferred, a ratio value  $\frac{r}{r_{\max}} = 0.56$ . The rate of overall change in  $\Delta$  is decreased for parameter set *II*, similar to the observations made for TO fragments (Fig. 2.6).

### **Pd<sub>887</sub>**

A selection of the most energetically favourable  $\Delta$  for Ih, I-Dh, CO, TO and M-Dh are plotted against  $N$  in Fig. 2.8, and compared to Pd<sub>887</sub>. Pd<sub>887</sub> is a cluster of recent experimental interest which is a magic number for M-Dh when  $(m, n, r) = (4, 5, 3)$ . As  $m \neq n$  the (100) faces seen in the centre of Fig. 2.2 increase in size forming (110) faces, though still with (100) atomic packing (Fig. 2.9). For parameter set *I* the Pd<sub>887</sub> cluster is 0.2 eV from the minimum, whilst for parameter set *II* this energy gap is much smaller (0.01 eV). In the experimental work of Pearmain [16], 86 % of 161 clusters were found to have irregular geometries, with small quantities of identifiable high-symmetry structures: 4 were identified as TO, whilst 5 more labelled as Ih, and only one as M-Dh. Whilst some of these limitations can be attributed to uncertainties in cluster orientation and experimental resolution limitations, the presence of several high-symmetry structures experimentally also indicates that these structures are close

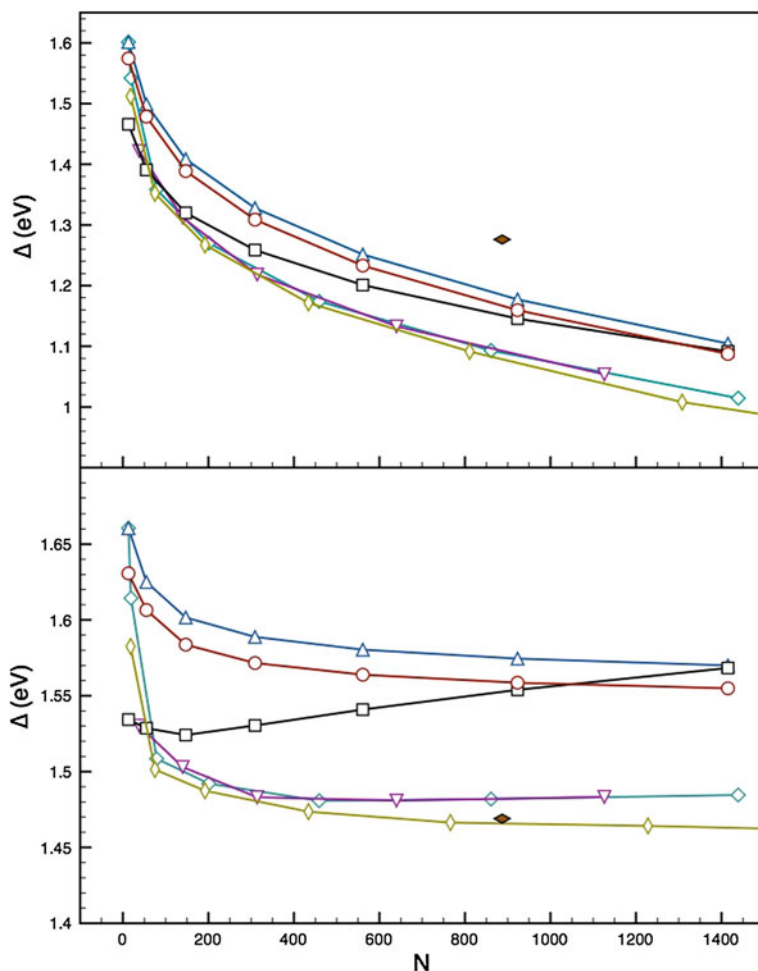


**Fig. 2.8** *Top*: Plot of  $\Delta$  for  $\text{Pd}_N$  structures against  $N$ , using parameter set *I* of Cleri and Rosato [12]. *Bottom*: As above, using parameter set *II* of Baletto et al. [2]. Ih (black squares), I-Dh (red circles), CO (blue upward triangles) are given, as well as the most energetically competitive atom-centred and void-centred TO (purple downward triangles and green diamonds, respectively), and M-Dh structures (yellow vertical diamonds).  $\text{Pd}_{887}$  is also shown (brown filled lateral diamond). Adapted from [55] by permission of the PCCP Owner Societies

in energy, and morphological changes under the electron beam are documented. Whilst the statistics provided from experiment is small, these experimental results fit to our calculations with parameter set *I*, where the energy gap to  $\text{Pd}_{887}$  is significantly large such that formation may only happen from kinetic trapping (not considering the impact the substrate may have on the structure).

Overall, Fig. 2.8 illustrates that parameter sets *I* and *II* have distinct energetic preference to the TO and M-Dh structures, compared to the Ih, I-Dh and CO. The Ih

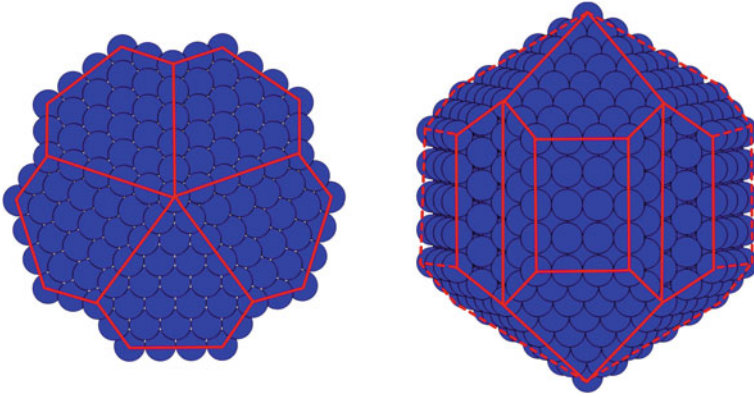


**Fig. 2.9** Image of  $\text{Pd}_{887}$  M-Dh structure, where  $(m, n, r) = (4, 5, 3)$ . *Left*: View down five-fold axis. *Right*: View orthogonal to (*left*). Main faces are marked with *solid lines*

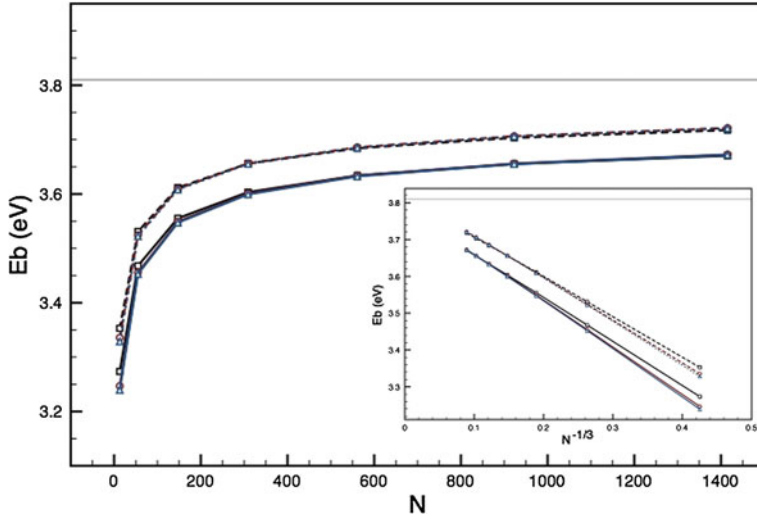
structure is competitive at low sizes ( $N < 100$ ), before becoming less favourable as  $N$  increases. There is distinct energy differences between the trend lines for the high-symmetry 12-vertex Ih, I-Dh and CO structures, and the lower symmetry TO and M-Dh structures, with the latter proving more energetically favourable. However, for both parameter sets the energy difference for  $\Delta$  is small between the TO/M-Dh trends and the 12-vertex Ih, I-Dh and CO structures ( $\sim 0.1$  eV), which equates to the thermal energy ( $k_b T$ ) when  $T \approx 1,200$  K, where  $T$  is temperature and  $k_b$  is the Boltzmann constant ( $8.617 \times 10^{-5}$  eV  $\text{K}^{-1}$ ). Though the energetic pathways between the different structures have not been calculated, we can be led to believe that transformation between these structures is not common under electron microscopy conditions, though subtler structural rearrangement have been observed [16].

### 2.4.2 $\text{Au}_N$ Clusters

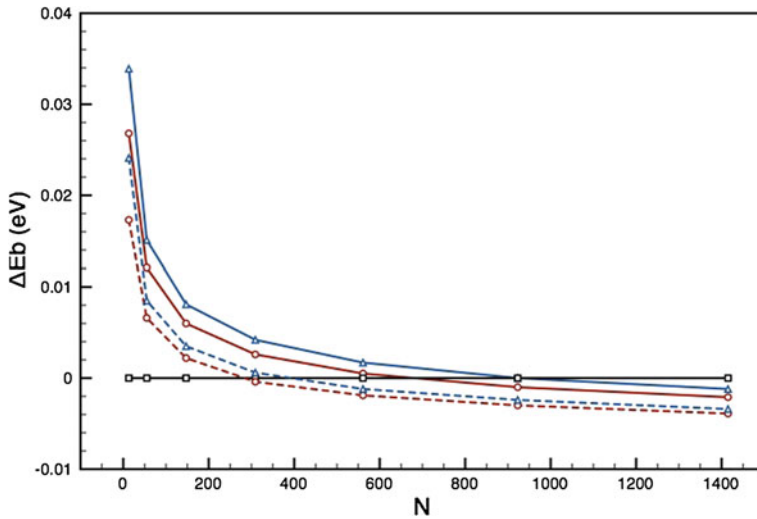
#### 12-Vertex Structures: Icosahedra, Ino-Decahedra and Cuboctahedra

Figure 2.10 compares  $E_b$  for the high-symmetry  $\text{Au}_N$  structures of the Ih, I-Dh and CO geometries. Similar trends to the results of  $\text{Pd}_N$  are seen with sharply increasing  $E_b$  for  $N < 100$ , levelling out asymptotically towards the bulk  $E_{coh}$  value of 3.81 eV [52] as  $N \rightarrow \infty$ . Parameter set II tends to a higher value of  $E_b$  than parameter set I, an inverse of the results for  $\text{Pd}_N$  clusters (Fig. 2.4). Attention to the inset, which relates  $E_b$  to the bulk limit ( $N^{-\frac{1}{3}} \rightarrow 0$ ), suggests that the parameter set I underestimates the extrapolated bulk  $E_{coh}$  value (3.77 eV), whilst parameter set II does not (3.81 eV).

Structural preferences are difficult to identify in Fig. 2.10; thus  $\Delta E_b$  is plotted in Fig. 2.11. For parameter set I we see intersection of  $E_{b_{Ih}}$  at  $N = 682$  by  $\Delta E_{b_{I-Dh}}$  and at  $N = 923$  by  $\Delta E_{b_{CO}}$ , calculated using a linear fit. For parameter set II



**Fig. 2.10** Main Plot of  $E_b$  for  $Au_N$  structures against  $N$ . Solid lines represent the parameter set I of Cleri and Rosato [12], and dashed lines represent the parameter set II of Baletto et al. [2]. Inset Plot of  $E_b$  for  $Au_N$  structures against  $N^{-1/3}$ . Ih (black squares), I-Dh (red circles) and CO (blue triangles) are shown in both plots; the bulk  $E_{coh}$  (3.81 eV [52]) is displayed as a grey solid line



**Fig. 2.11** Plot of  $\Delta E_b$  for Ih (black), I-Dh (red) and CO (blue)  $Au_N$  structures against  $N$ . Solid lines represent parameter set I of Cleri and Rosato [12], and dashed lines represent parameter set II of Baletto et al. [2]



these intersections of  $E_{bIh}$  are at lower  $N$ : 284 and 393 for  $\Delta E_{bI-Dh}$  and  $\Delta E_{bCO}$ , respectively. The values of  $N$  for these intersections are much less than found for  $Pd_N$ , implying relative instability of the close-packed cluster geometries (Ih, I-Dh) with respect to the crystalline bulk fragments for Au nanoparticles.

## FCC Structures

Comparison of the CO structures with a variety of other FCC fragments (Fig. 2.12) leads to the observation that the CO structure is not the optimal for the FCC fragments, identical to findings for Pd. Whilst a large spread of energetic values have been identified ( $0.8 < \Delta < 2$  eV), some higher in energy than the CO, the energetic minima and associated trend lines are approximately 0.1 eV lower in energy than for the CO structures. Of particular interest is the positive gradient seen for the energy trend line of parameter set *I*, with values reaching a minimum at  $\Delta = 1.269$  eV for  $N = 79$  ( $n_l = 5$ ,  $n_{cut} = 1$ ), before rising towards 1.5 eV. This case is not the same for the parameter set *II*, where a plateau is reached for  $N > 1,000$  at  $\Delta \sim 0.95$  eV. Quantitatively, the  $\Delta$  values of parameter set *I* are greater than those of parameter set *II*. The minimum atom-centred and void-centred geometries are closely competitive in energy for both parameter sets; further analysis shows that the preferred structures maximise the hexagonal (111)-packed surfaces, whilst minimising exposed (100) surfaces. This observation can be linked to the surface energies of the (111) and (100) surfaces for Au, which have previously been reported by Uppenbrink et al. as 93.2 and 97.1 meV  $\text{\AA}^{-2}$ , respectively [56], thus favouring Au (111) facet formation over (100).

## Marks-Decahedra

M-Dh structures have been generated, using systematic variation of  $m$ ,  $n$  and  $r$ , and minimised using both parameter sets:  $\Delta$  has been plotted in Fig. 2.13 for the series of structures  $Au_N$ . Similar to the case of  $Pd_N$ , we find that fully stellated M-Dh structures are unfavourable (except inevitably for  $Au_{18}$  when  $m = n = r = 1$ , as truncation is not possible). The formation of truncated features is favourable compared to the simple I-Dh clusters, but the ratio  $\frac{r}{r_{max}}$  tends to be smaller than previously seen for  $Pd_N$  at large  $N$ , indicating that large stellated growths on the (100) faces, truncated or not, are generally not energetically suitable; e.g. for  $r_{max} = 9$  a truncation of the edges such that  $m = n = 7$ ,  $r = 3$ . The trend lines for each value of  $r_{max}$  are similar to  $Pd_N$ , i.e. they are steeper sided funnels at low  $N$ , which tend to flatten out as  $N \rightarrow 6,000$ . The results values using parameter set *I* rise above those of parameter set *II*, a reverse of the trend for  $Pd_N$  M-Dh structures in Fig. 2.7, and similar to our observations noted for Figs. 2.10, 2.11 and 2.12 in relation to the energetic ordering of parameter sets *I* and *II*. We also note here that  $\Delta$  increases with  $N$  for parameter set *I*, similar to the top of Fig. 2.12.

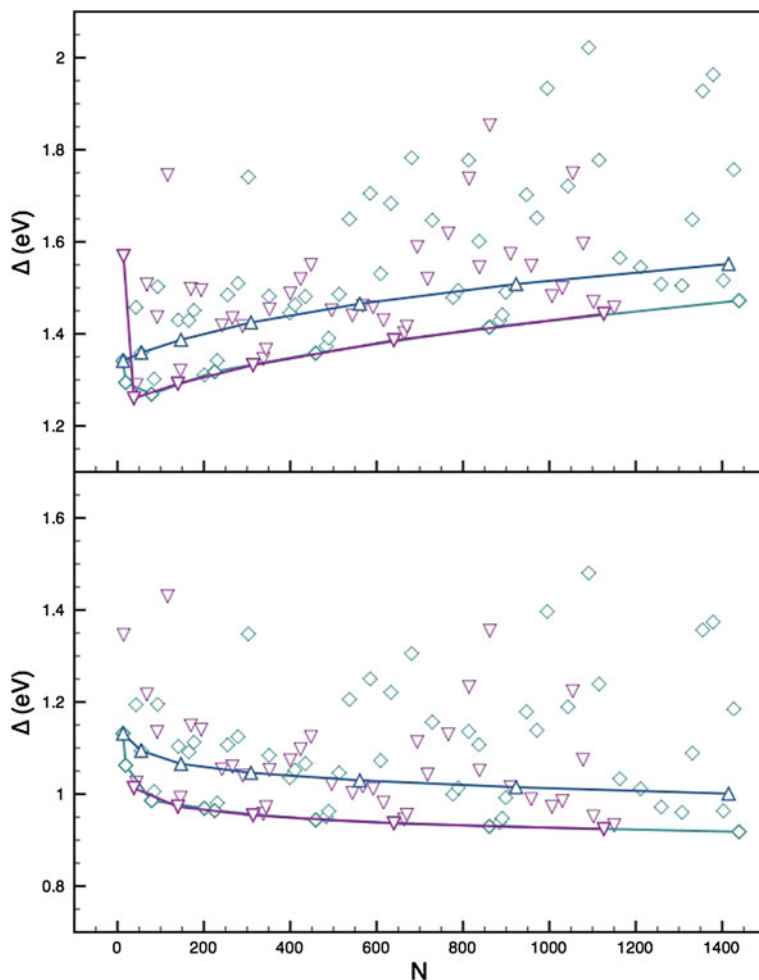


**Fig. 2.12** *Top:* Plot of  $\Delta$  against  $N$  for various TO  $\text{Au}_N$  structures, where  $N < 1,500$ , for parameter set *I* of Cleri and Rosato [12]. *Bottom:* As above, using parameter set *II* of Baletto et al. [2]. FCC structures with an atom at their centre (green diamonds) and with a void at their centre (purple triangles) are plotted against the CO structure (blue upwards triangles) of increasing shell size  $k$ . Lines are plotted to show the lowest values for each structure type. Reproduced from [55] by permission of the PCCP Owner Societies

### **Au<sub>887</sub>**

A selection of the most energetically favourable  $\Delta$  for Ih, I-Dh, CO, TO and M-Dh are plotted against  $N$  in Fig. 2.14, and compared to Au<sub>887</sub>. Similar to Pd<sub>887</sub>, Au<sub>887</sub> has been the subject of recent experimental interest [35]. For both parameter sets *I* and *II* we find that  $\Delta$  for the 12-vertex high-symmetry structures (Ih, I-Dh and CO)

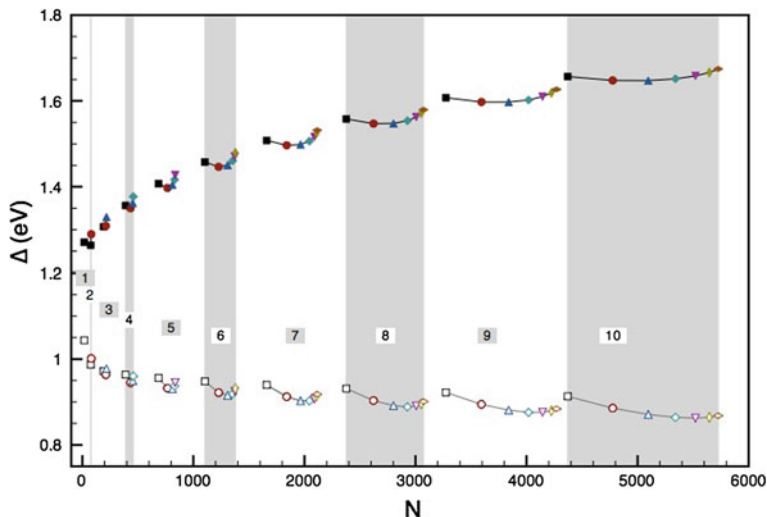


**Fig. 2.13** Plot of  $\Delta$  against  $N$  for  $Au_N$  M-Dh of varying re-entrant sizes. Structures have been created such that  $r < 9$ , and  $m = n < 11$  where  $r = 2$  (black squares), 3 (red circles), 4 (blue upward triangles), 5 (green diamonds), 6 (purple downward triangles), 7 (yellow laterally-extended diamonds) and 8 (brown vertically-extended diamonds) are displayed. Parameter set *I*, of Cleri and Rosato [12], is plotted with closed symbols and black trend lines, and parameter set *II*, of Baletto et al. [2], is plotted with open symbols and grey trend lines. Trend lines illustrate the effect of reduced truncation of the stellated features from an I-Dh core ( $r = 1$ ) to fully stellated structures ( $m = 1$ ). Background colouring is added to highlight distinct trend lines.  $r_{max}$  is also labelled from 1 to 10. Reproduced from [55] by permission of the PCCP Owner Societies

is 0.1 eV greater than the most stable FCC and M-Dh structures, and that  $Au_{887}$  is energetically closer to the latter. The Ih structure is closely competitive for  $N < 100$ , before becoming strongly unfavourable for  $N > 500$ .  $\Delta$  for the other investigated structures run parallel to each other for  $N > 200$  for both parameter sets; below this they are closer in energy, though one would also suspect that there are many other alternative structures which we have not investigated here which may be competitive. The heat required for direct thermal transformation from Ih/I-Dh/CO to M-Dh/TO is again in the range of  $T \approx 1,200$  K. This value is sufficiently high that we would not expect structural rearrangement in ambient experimental conditions; for smaller ( $N < 100$ ) this is not the case and structural evolution under an electron beam has been documented [32].

### 2.4.3 $(Au_{core}Pd_{shell})_N$ Clusters

With the 12-vertex high-symmetry structures it is possible to conduct systematic studies of their core/shell bimetallic structures by building up clusters with layers

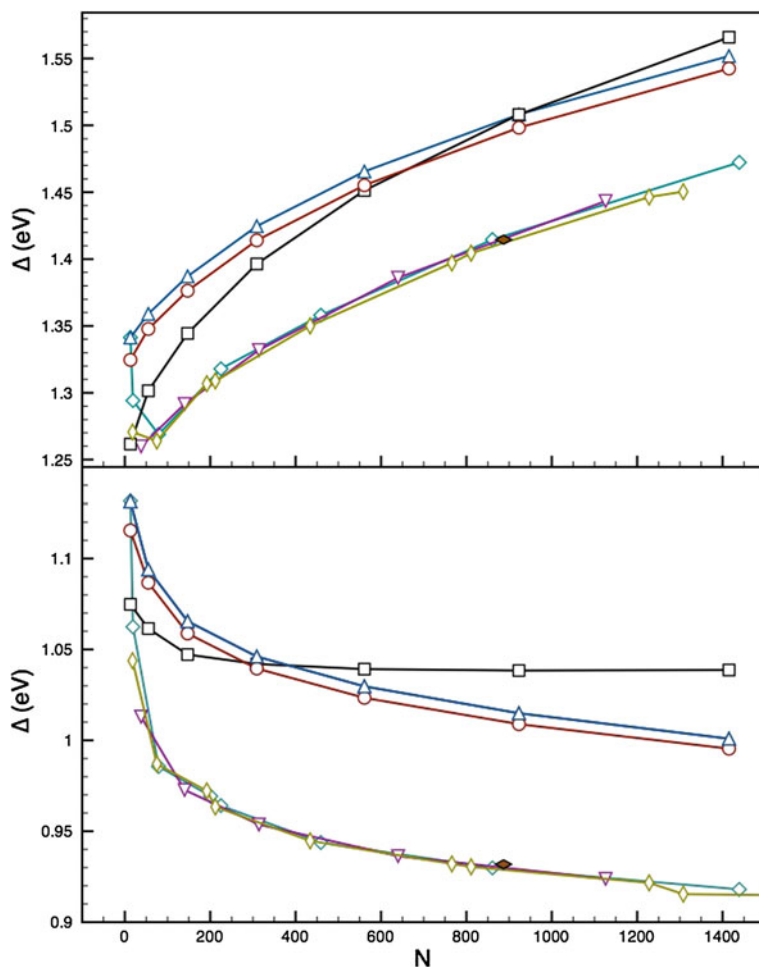


**Fig. 2.14** *Top:* Plot of  $\Delta$  for  $\text{Au}_N$  structures against  $N$ , using parameter set *I* of Cleri and Rosato [12]. *Bottom:* As above, using parameter set *II* of Baletto et al. [2]. Ih (black squares), I-Dh (red circles), CO (blue upward triangles) are given, as well as the most energetically competitive atom-centred and void-centred TO (purple downward triangles and green diamonds, respectively), and M-Dh structures (yellow vertical diamonds).  $\text{Au}_{887}$  is also shown (brown filled lateral diamond, black edges). Adapted from [55] by permission of the PCCP Owner Societies

of different atom types. One of the more fundamental cluster structures is that of core/shell segregation, whereby one element occupies sites close to the core of the cluster and another element occupies more surface sites. This kind of arrangement is commonly documented experimentally for  $(\text{AuPd})_N$  [3, 57]. By creating a fixed core of one element and nuclearity, and growing shells of another element on the surface (Fig. 2.15), we are able to compare the relative stability of the core/shell bimetallic systems with respect to the homogeneous monometallic systems, and also

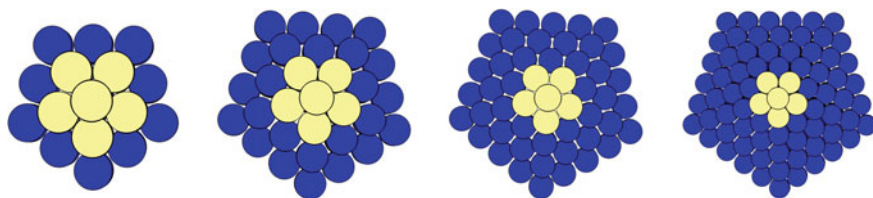


**Fig. 2.15** Cross section of  $(\text{Au}_{\text{core}}\text{Pd}_{\text{shell}})_N$  Dh with a fixed core of 13 atoms ( $k = 1$ ). Left to right:  $N = 55, 147, 309$  and  $561$ , respectively. Pd and Au are represented in *blue* and *yellow*, respectively. Reproduced from [46] by permission of The Royal Society of Chemistry

the relative stability of the different core/shell structures to each other, i.e. the Ih, I-Dh and CO. Naively, one could expect a linear transition between the structural preferences of Au and Pd as we are using arithmetic means for the Au-Pd interaction.

Comparison of  $\Delta$  for the pure clusters offers initial insight into the predicted energetic evolution with the addition of a second element to the cluster: Fig. 2.16 gives  $\Delta$  for the Ih, I-Dh and CO values for  $\text{Au}_N$  and  $\text{Pd}_N$  clusters. For parameter set *I* we notice that for  $N < 150$  the  $\text{Au}_N$  structures have a lower  $\Delta$  than  $\text{Pd}_N$ , however this does not hold true for  $N > 200$ , with  $\text{Pd}_N$  becoming energetically preferred and the gap between the trend lines increasing up to  $N = 1,500$ . For parameter set *II* the  $\text{Au}_N$  structures remain more energetically stable compared to those of  $\text{Pd}_N$ , with the gap between the two remaining constant at  $\sim 0.5$  eV. As discussed previously, the Ih structure is favoured to large  $N$  for  $\text{Pd}_N$ , unlike  $\text{Au}_N$ , and this is shown for both parameter sets.

Ih, I-Dh and CO clusters were generated with fixed-size Au cores and Pd layering added to form the shell, as illustrated in Fig. 2.15. Results from parameter set *I* and *II* have been plotted in Fig. 2.17 and 2.18, respectively. In Fig. 2.17 comparison with  $\text{Pd}_N$  shows that adding the Au impurity results in an increase in  $E_{\text{exc}}$ , and thus  $\Delta$ , for all clusters; and the greater the concentration of Au in the core of the structure, the greater this difference is between  $\Delta$  for  $\text{Pd}_N$  and  $(\text{Au}_{\text{core}}\text{Pd}_{\text{shell}})_N$ . Though not plotted, comparison with  $\text{Au}_N$  also shows that  $\Delta$  for  $(\text{Au}_{\text{core}}\text{Pd}_{\text{shell}})_N$  is increased with respect to  $\text{Au}_N$  when the number of Pd layers is small ( $k < 4$ ), making this form of mixing not preferable for the bimetallic system at low nuclearities. Larger clusters appear more stable, with  $\Delta$  for the bimetallic cluster falling between the pure clusters, and the difference in  $\Delta$  between  $\text{Pd}_N$  and  $(\text{Au}_{\text{core}}\text{Pd}_{\text{shell}})_N$  decreasing as  $N$  increases. We also note that for a core of  $\text{Au}_{55}$  or greater the Ih is no longer the preferred structure with respect to the I-Dh and CO; this is in-keeping with the observed trends for the pure  $\text{Au}_N$  clusters.

For parameter set *II* (Fig. 2.18), this destabilised effect is not so prominent. Whilst thin (monolayer) Pd shells are not energetically favourable, especially for increasing size of the  $\text{Au}_N$  core, multiple Pd layers have a quenching effect on this disparity, reducing  $E_{\text{exc}}$  such that for an  $\text{Au}_{13}$  core with three layers of Pd or greater ( $k > 3$ ) it appears more energetically favourable than the  $\text{Pd}_N$  clusters, though not also the  $\text{Au}_N$  clusters.

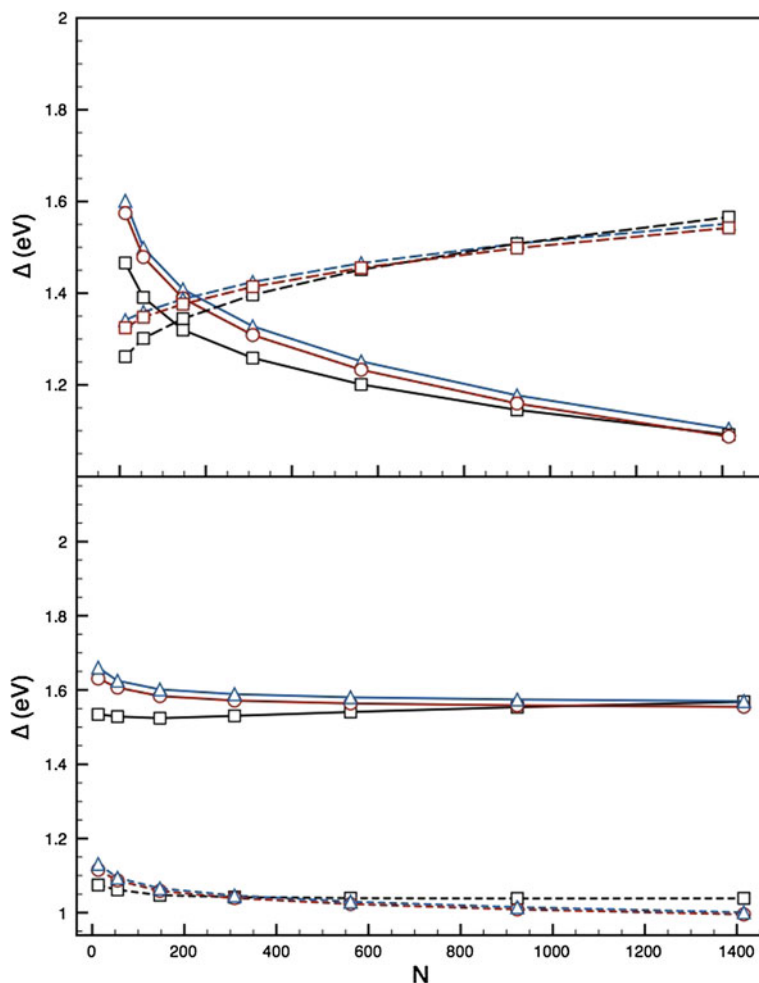


**Fig. 2.16** *Top:* Plot of  $\Delta$  against  $N$  for the 12-vertex high-symmetry structures, using parameter set *I* of Cleri and Rosato [12]. *Bottom:* As above, using parameter set *II* of BALETTO et al. [2]. Ih (black squares), I-Dh (red circles) and CO (blue triangles) are shown, with Pd<sub>N</sub> (solid lines) and Au<sub>N</sub> (dashed lines) plotted. Reproduced from [46] by permission of The Royal Society of Chemistry

#### 2.4.4 (Pd<sub>core</sub>Au<sub>shell</sub>)<sub>N</sub> Clusters

Using parameter set *I* and inverting the core-shell segregation to form (Pd<sub>core</sub>Au<sub>shell</sub>)<sub>N</sub> leads to the reverse effect of that witnessed for the (Au<sub>core</sub>Pd<sub>shell</sub>)<sub>N</sub>: the value of  $\Delta$  tends to decrease with respect to the pure clusters (Fig. 2.19) as the size of the Pd core increases. The effect is greatest for smaller clusters, with monolayers of Au, with the difference between  $\Delta$  of the core/shell and pure clusters reducing as  $N$  increases, for a fixed core. For multiple Au shell layers  $\Delta$  shifts to a value

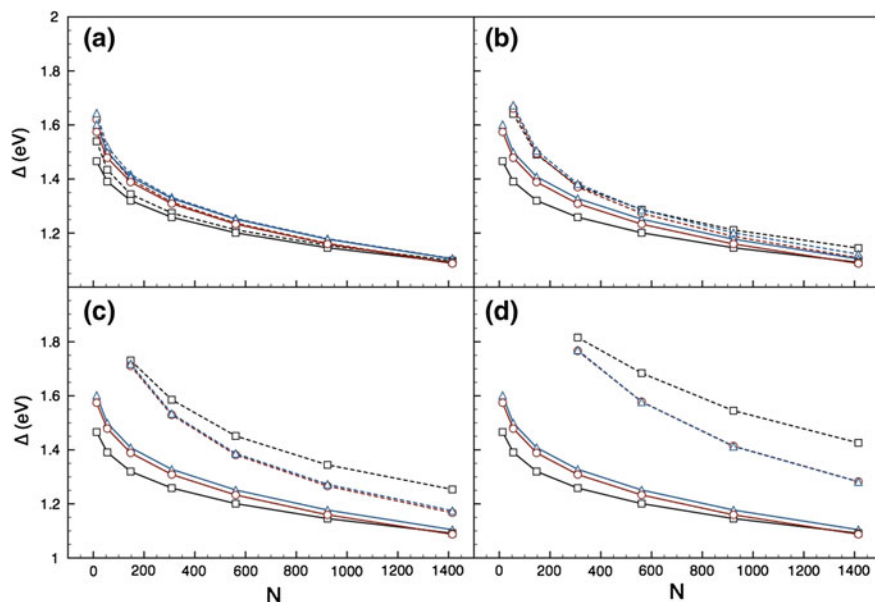


**Fig. 2.17** Plots of  $\Delta$  against  $N$  for the  $\text{Au}_{\text{core}}\text{Pd}_{\text{shell}}$  12-vertex high-symmetry structures (*dashed lines*), using parameter set *I* of Cleri and Rosato [12], with cores: **a**  $\text{Au}_1$  **b**  $\text{Au}_{13}$  **c**  $\text{Au}_{55}$  **d**  $\text{Au}_{147}$ . Ih (black squares), I-Dh (red circles) and CO (blue triangles) are shown, with  $\text{Pd}_N$  (solid lines) also plotted. Reproduced from [46] by permission of The Royal Society of Chemistry

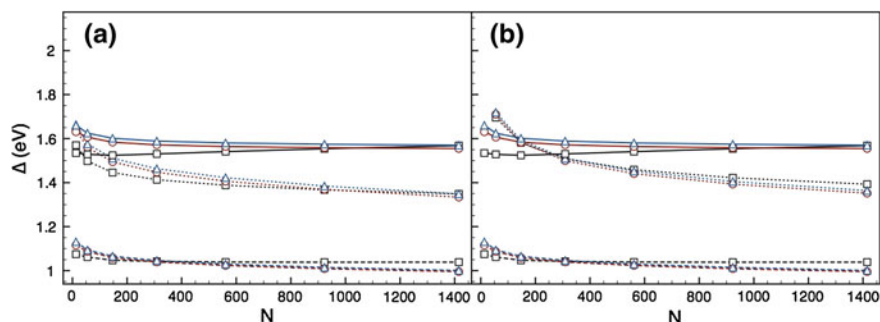


**Fig. 2.18** Plots of  $\Delta$  against  $N$  for the  $\text{Au}_{\text{core}}\text{Pd}_{\text{shell}}$  12-vertex high-symmetry structures (*dotted lines*), using parameter set *II* of Baletto et al. [2], with cores: **a**  $\text{Au}_1$  and **b**  $\text{Au}_{13}$ . Ih (black squares), I-Dh (red circles) and CO (blue triangles) are shown, with  $\text{Pd}_N$  (solid lines) and  $\text{Au}_N$  (dashed lines) also plotted. Reproduced from [46] by permission of The Royal Society of Chemistry

between the pure values, illustrating again the averaging effect we spoke of previously. Figure 2.19 also shows that the Ih structure becomes distinctly more preferable than the I-Dh and CO structures, whilst the energy gap between the I-Dh and CO also increases. For a core of  $\text{Pd}_{55}$  or greater the transition from Ih to I-Dh and CO is out of the nuclearity range studied (i.e.  $N > 1,500$ ).

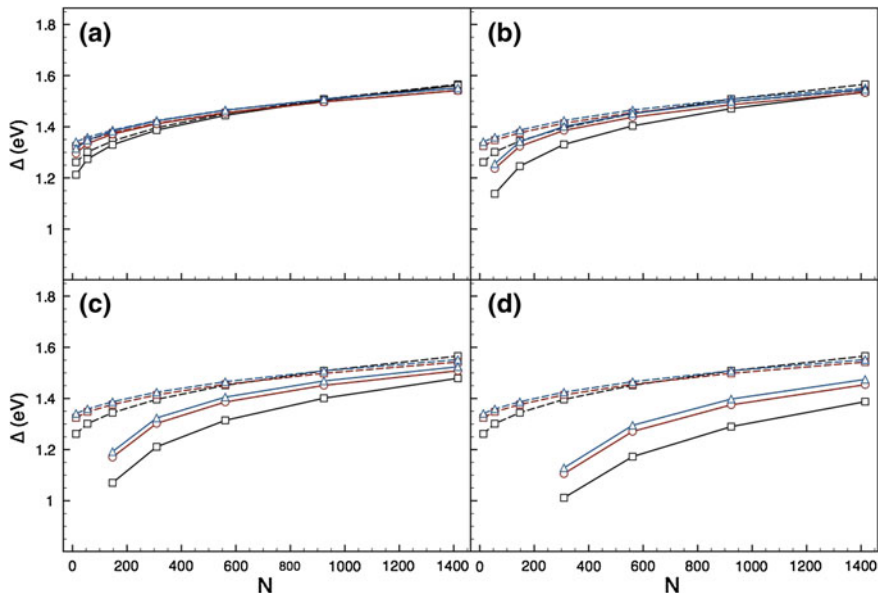


**Fig. 2.19** Plots of  $\Delta$  against  $N$  for the  $\text{Pd}_{\text{core}}\text{Au}_{\text{shell}}$  12-vertex high-symmetry structures (solid lines), using parameter set *I* of Cleri and Rosato [12], with cores: **a**  $\text{Pd}_1$  **b**  $\text{Pd}_{13}$  **c**  $\text{Pd}_{55}$  **d**  $\text{Pd}_{147}$ . Ih (black squares), I-Dh (red circles) and CO (blue triangles) are shown, with  $\text{Au}_N$  (dashed lines) also plotted

For parameter set *II* the effect of multiple Au layers is not so favourable (Fig. 2.20). Small Pd impurities in the core of small Au clusters are energetically favourable, compared to the pure  $\text{Pd}_N$  clusters, but not compared to the  $\text{Au}_N$  clusters. For all core sizes, an Au coating becomes unfavourable with respect to the pure clusters when thicker than a monolayer, and increases with thicker Au coverage, illustrating that the segregation we have used may not be as preferable as a mixed alloy with these parameters, similar to results seen by Ismail et al. [39].

Attention to the relative stability of the  $(\text{Pd}_{\text{core}}\text{Au}_{\text{shell}})_N$  structures with just a monolayer coating, as shown in Fig. 2.21, shows an unusually high stability which increases with  $N$  (Fig. 2.22) for both parameter sets *I* and *II*.

A monolayer coating of Au on a Pd core, with parameter set *I*, results in  $\Delta$  less than for both  $\text{Au}_N$  and  $\text{Pd}_N$  clusters of the same nuclearity. This is a strong indication of the preference of the stability of the  $\text{Pd}_{\text{core}}\text{Au}_{\text{shell}}$  segregation, and agrees with the common discovery of core-shell structures in previous structural searches [38, 39]. The difference between the energy of the  $\text{Pd}_N$  and the  $(\text{Pd}_{\text{core}}\text{Au}_{\text{shell}})_N$  remains constant as  $k$  increases, at a gap of  $\sim 0.3$  eV. The Ih structure is energetically preferable throughout, in stark contrast to the same calculations for the  $\text{Au}_N$  clusters which show an early tendency to adopt crystalline structures.

For parameter set *II* a monolayer coating has a similar effect in stabilising the  $\text{Pd}_N$  cluster. However, for  $N < 800$  ( $k < 6$ ) the  $(\text{Pd}_{\text{core}}\text{Au}_{\text{shell}})_N$  clusters are less stable



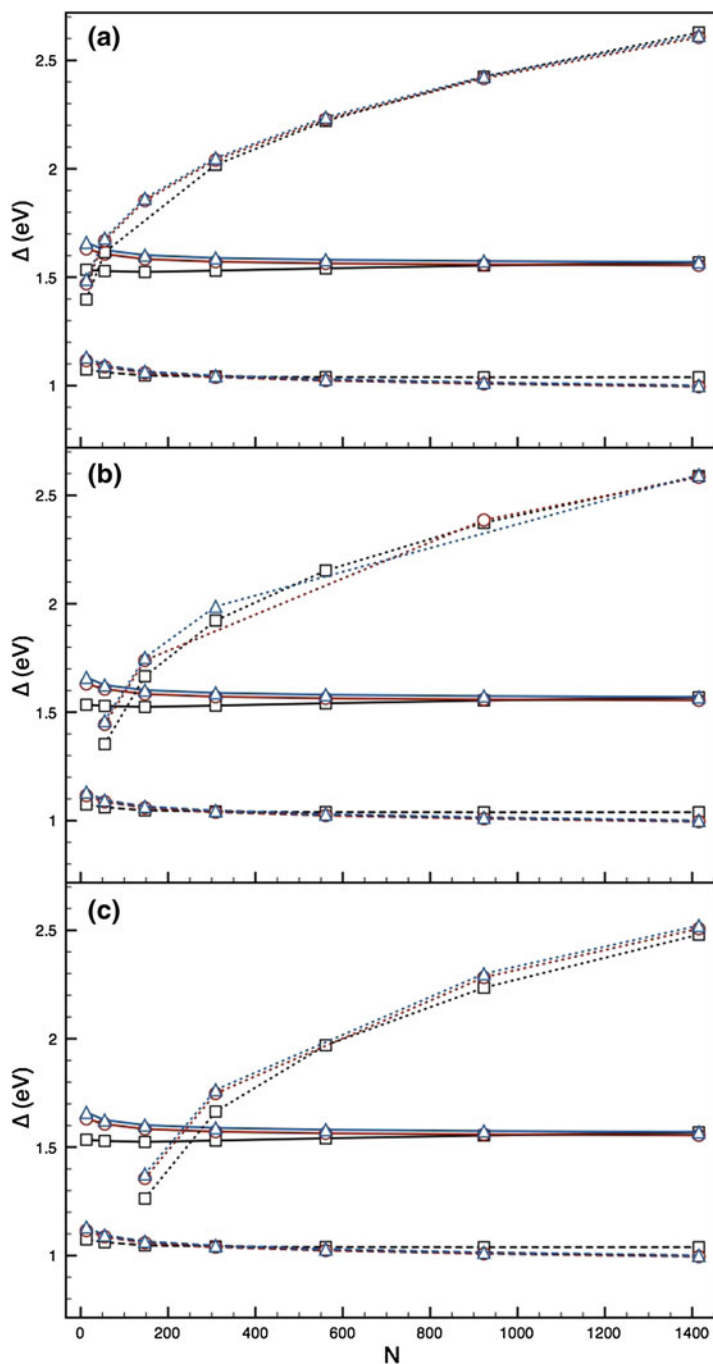


**Fig. 2.20** Plots of  $\Delta$  against  $N$  for the  $\text{Pd}_{\text{core}}\text{Au}_{\text{shell}}$  12-vertex high-symmetry structures (dotted lines), using parameter set II of Baletto et al. [2], with cores: **a**  $\text{Pd}_1$  **b**  $\text{Pd}_{13}$  **c**  $\text{Pd}_{55}$ . Ih (black squares), I-Dh (red circles) and CO (blue triangles) are shown, with  $\text{Au}_N$  (dashed lines) and  $\text{Pd}_N$  (solid lines) also plotted. Reproduced from [46] by permission of The Royal Society of Chemistry

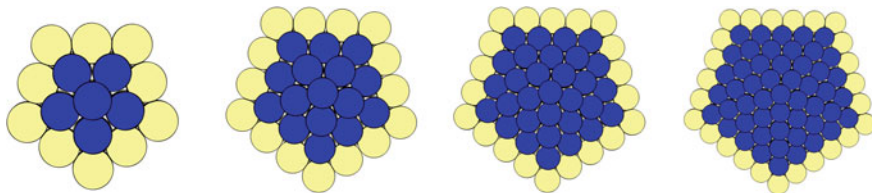


**Fig. 2.21** Cross section of  $(\text{Pd}_{\text{core}}\text{Au}_{\text{shell}})_N$  Dh with a monolayer covering on the shell. *Left to right*:  $N = 55, 147, 309$  and  $561$ , respectively. Pd and Au are represented in *blue* and *gold*, respectively. Reproduced from [46] by permission of The Royal Society of Chemistry

than the pure  $\text{Au}_N$  clusters. For  $N > 800$  the core/shell segregation becomes more energetically favourable than the pure  $\text{Au}_N$  cluster; this implies that this segregation is not-preferable at low  $N$ , where mixing is perhaps preferred, but as  $N$  increases, and so the ratio of Pd to Au atoms increases in favour of Pd, so does the suitability of core/shell segregation to this structure. This is perhaps the driving force behind the structural rearrangements seen in previous molecular dynamics studies [41], where core/shell inversion occurs. As the difference in  $\Delta$  between the pure clusters and  $(\text{Pd}_{\text{core}}\text{Au}_{\text{shell}})_N$  is increasing, we can predict that as  $N$  increases beyond  $N = 1,500$  that this structural arrangement may become even more favourable, as it minimises  $E_{\text{exc}}$ .

## 2.5 Conclusions

We have studied the stabilities of high-symmetry  $\text{Au}_N$ ,  $\text{Pd}_N$  and  $(\text{AuPd})_N$  clusters, using mathematical constructs, a semi-empirical potential with two different parameter sets, and a quasi-newtonian minimisation technique. The structures for which calculations were performed include the Ih, I-Dh, CO, M-Dh and FCC fragments; this list is by no means exhaustive but does give a good insight to the preferred nanocluster packing in high-symmetry structures.

For  $\text{Pd}_N$  clusters both parameter sets tested result in preferences for the Ih structures for  $N < 1,000$  over other high-symmetry 12-vertex geometries. However, TO  $\text{Pd}_N$  clusters with reduced (100) exposure, and M-Dh  $\text{Pd}_N$  clusters with truncation stellations prove to have lower  $E_{\text{exc}}$ , as a result of the reduced (100) surfaces.  $\text{Pd}_{887}$  proves to be competitive with M-Dh and TO structures when using parameter set *II*; this is not the case for parameter set *I* where  $\text{Pd}_{887}$  is similar in  $\Delta$  to the 12-vertex structures. Overall, the parameters of Cleri and Rosato tend towards values of  $E_b$  greater than the parameters of Baletto et al., with extrapolation to the bulk limit illustrating the latter gives results closer to the experimentally measured value.

For  $\text{Au}_N$  clusters we found a tendency towards FCC structures at values of  $N$  lower than seen for  $\text{Pd}_N$ : the parameters of Cleri and Rosato gave a transition at  $N \approx 650$  to the I-Dh, whilst for the parameters of Baletto et al. this value was lower

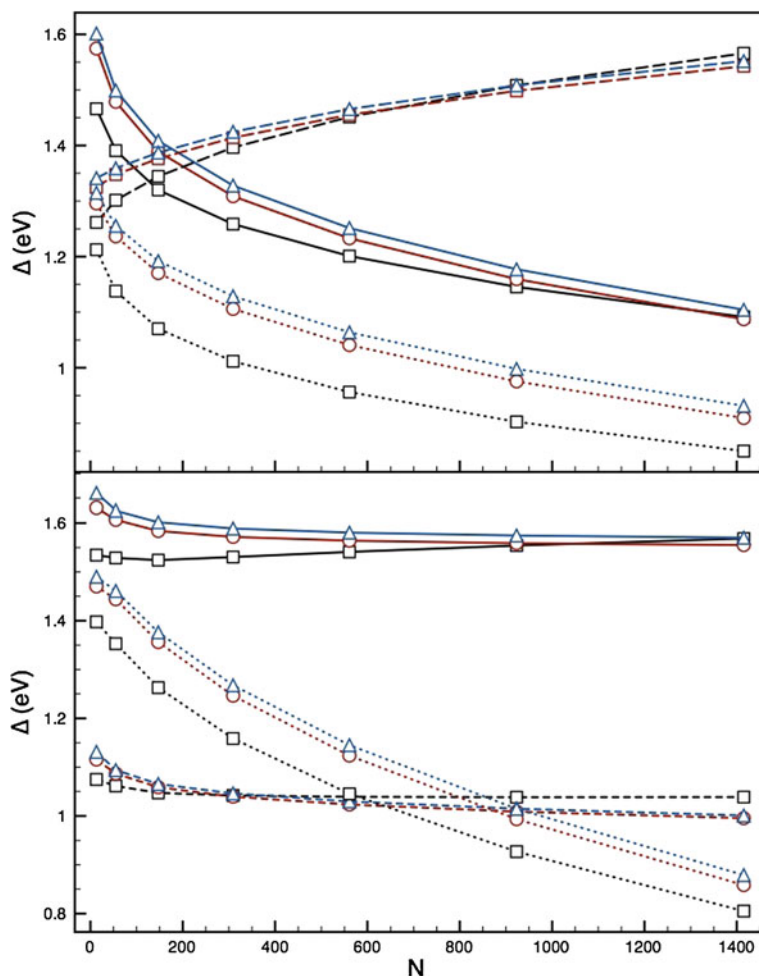


**Fig. 2.22** *Top:* Plots of  $\Delta$  against  $N$  for the  $\text{Au}_{\text{core}}\text{Pd}_{\text{shell}}$  12-vertex high-symmetry structures, using parameter set *I* of Cleri and Rosato [12], with a monolayer covering of Au. *Bottom:* As above, using parameter set *II* of Baletto et al. [57]. Ih (black squares), I-Dh (red circles) and CO (blue triangles) are shown;  $\text{Pd}_N$  (solid lines),  $\text{Au}_N$  (dashed lines) and  $\text{Pd}_{\text{core}}\text{Au}_{\text{shell}}$  (dotted lines) are plotted. Reproduced from [46] by permission of The Royal Society of Chemistry

still. TO and M-Dh structures again prove more stable than the 12-vertex geometries, with shrinking of the (100) faces favourable.  $\text{Au}_{887}$  is competitive with the energetic minima for both parameter sets, offering enthusiasm for further experimental work trying to identify this structure. Overall, the parameters of Baletto et al. give a larger value of  $E_b$  at low  $N$  than the parameters of Cleri and Rosato.

For  $(\text{AuPd})_N$  clusters we found that the preferred arrangement is for  $(\text{Pd}_{\text{core}}\text{Au}_{\text{shell}})_N$  for both parameter sets, with thin (monolayer) surface coverings of Au

being most energetically favourable compared to the homogeneous clusters; this is highly compatible with the experimental measurements  $E_{surf}(\text{Pd}) > E_{surf}(\text{Au})$  and  $E_{coh}(\text{Pd}) > E_{coh}(\text{Au})$ . For the parameters of Baletto et al. multiple layers of Au lead to energetic instability, with  $\Delta$  values greater than for either of the pure metal nanoparticles; the same is not the case for the parameters of Cleri and Rosato.  $(\text{Au}_{core}\text{Pd}_{shell})_N$  clusters are not energetically favourable with thin coatings of Pd, however as the shell coating thickens so the stability improves. This effect is more prominent for the parameters of Cleri and Rosato. Ih structures are not favourable compared to the I-Dh and CO for  $(\text{Au}_{core}\text{Pd}_{shell})_N$ , where as they are strongly preferred for  $(\text{Pd}_{core}\text{Au}_{shell})_N$ . Overall, the strong tendency towards core/shell segregation is emphasised for the parameters of Cleri and Rosato [12], and not so much for the parameters of Baletto et al. [2], agreeing with previous observations for smaller  $(\text{AuPd})_N$  clusters [38, 39].

Exploring other high-symmetry homotops for the bimetallic  $(\text{AuPd})_N$  clusters is necessary in the future to know whether other segregated formations are more favourable than those postulated here, with investigation into other lower-symmetry structures also required to give a more complete treatment of structural preference in any future work.

## References

1. R.L. Johnston, *Atomic and Molecular Clusters* (Taylor and Francis, London, 2002)
2. F. Baletto, R. Ferrando, A. Fortunelli, F. Montalenti, C. Mottet, Crossover among structural motifs in transition and noble-metal clusters. *J. Chem. Phys.* **116**(9), 3856–3863 (2002)
3. R. Ferrando, J. Jellinek, R.L. Johnston, Nanoalloys: from theory to applications of alloy clusters and nanoparticles. *Chem. Rev.* **108**(3), 845–910 (2008)
4. F. Baletto, R. Ferrando, Structural properties of nanoclusters: energetic, thermodynamic, and kinetic effects. *Rev. Mod. Phys.* **77**, 371–423 (2005)
5. P. Nava, M. Sierka, R. Ahlrichs, Density functional study of palladium clusters. *Phys. Chem. Chem. Phys.* **5**, 3372–3381 (2003)
6. G. Valerio, H. Toulhoat, Atomic sulfur and chlorine interaction with  $\text{Pd}_n$  clusters ( $n = 1-6$ ): a density functional study. *J. Phys. Chem. A* **101**(10), 1969–1974 (1997)
7. B. Kalita, R.C. Deka, Stability of small  $\text{Pd}_n$  ( $n = 1-7$ ) clusters on the basis of structural and electronic properties: a density functional approach. *J. Chem. Phys.* **127**(24), 244306–244316 (2007)
8. D.R. Jennison, P.A. Schultz, M.P. Sears, Ab initio calculations of Ru, Pd, and Ag cluster structure with 55, 135, and 140 atoms. *J. Chem. Phys.* **106**(5), 1856–1862 (1997)
9. R. Guirado-López, M.C. Desjonquères, D. Spanjaard, Tight-binding study of relaxation in  $\text{Rh}_N$  and  $\text{Pd}_N$  clusters ( $9 < N < 165$ ). *Phys. Rev. B* **62**(19), 13188–13195 (2000)
10. F. Aguilera-Granja, A. Vega, J. Rogan, G. Garcia, Metallic behavior of Pd atomic clusters. *Nanotechnology* **18**(36), 365706–365711 (2007)
11. N. Watari, S. Ohnishi, Atomic and electronic structures of  $\text{Pd}_{13}$  and  $\text{Pt}_{13}$  clusters. *Phys. Rev. B* **58**(3), 1665–1677 (1998)
12. F. Cleri, V. Rosato, Tight-binding potentials for transition metals and alloys. *Phys. Rev. B* **48**(1), 22–33 (1993)
13. V. Rosato, M. Guillope, B. Legrand, Thermodynamical and structural properties of FCC transition metals using a simple tight-binding model. *Philos. Mag. A* **59**(2), 321–336 (1989)

14. M. José-Yacamán, M. Marin-Almazo, J.A. Ascencio, High resolution TEM studies on palladium nanoparticles. *J. Mol. Catal. A* **173**(1–2), 61–74 (2001)
15. M. José-Yacamán, J.A. Ascencio, H.B. Liu, J. Gardea-Torresdey, Structure shape and stability of nanometric sized particles. *J. Vac. Sci. Technol. B* **19**(4), 1091–1103 (2001)
16. S.M. Morton, D.W. Silverstein, L. Jensen, Theoretical studies of plasmonics using electronic structure methods. *Chem. Rev.* **111**, 3962–3994 (2011)
17. G. Bravo-Perez, I.L. Garzan, O. Novaro, Non-additive effects in small gold clusters. *Chem. Phys. Lett.* **313**(3–4), 655–664 (1999)
18. J. Wang, G. Wang, J. Zhao, Density-functional study of  $Au_n$  ( $n=2-20$ ) clusters: lowest-energy structures and electronic properties. *Phys. Rev. B* **66**(3), 35418–35424 (2002)
19. V. Bonačić-Koutecký, J. Burda, R. Mitrić, M. Ge, G. Zampella, P. Fantucci, Density functional study of structural and electronic properties of bimetallic silver-gold clusters: comparison with pure gold and silver clusters. *J. Chem. Phys.* **117**(7), 3120–3131 (2002)
20. J. Li, X. Li, H.J. Zhai, L.S. Wang,  $Au_{20}$ : a tetrahedral cluster. *Science* **299**(5608), 864–867 (2003)
21. J. Wang, G. Wang, J. Zhao, Structures and electronic properties of  $Cu_{20}$ ,  $Ag_{20}$ , and  $Au_{20}$  clusters with density functional method. *Chem. Phys. Lett.* **380**, 716–720 (2003)
22. K. Michaelian, N. Rendón, I.L. Garzón, Structure and energetics of Ni, Ag, and Au nanoclusters. *Phys. Rev. B* **60**, 2000–2010 (1999)
23. C.L. Cleveland, U. Landman, M.N. Shafigullin, P.W. Stephens, R.L. Whetten, Structural evolution of larger gold clusters. *Z. Phys. D* **40**, 503–508 (1997)
24. N.T. Wilson, R.L. Johnston, Modelling gold clusters with an empirical many-body potential. *Eur. Phys. J. D.* **12**(1), 161–169 (2000)
25. M.M. Alvarez, J.T. Khoury, T.G. Schaaff, M.N. Shafigullin, I. Vezmar, R.L. Whetten, Optical absorption spectra of nanocrystal gold molecules. *J. Phys. Chem. B* **101**(19), 3706–3712 (1997)
26. H. Häkkinen, R.N. Barnett, U. Landman, Electronic structure of passivated  $Au_{38}(SCH_3)_{24}$  nanocrystal. *Phys. Rev. Lett.* **82**(16), 3264–3267 (1999)
27. H. Häkkinen, M. Walter, H. Grönbeck, Divide and protect: capping gold nanoclusters with molecular gold-thiolate rings. *J. Phys. Chem. B* **110**(20), 9927–9931 (2006)
28. J. Akola, M. Walter, R.L. Whetten, H. Häkkinen, H. Grönbeck, On the structure of thiolate-protected  $Au_{25}$ . *J. Am. Chem. Soc.* **130**(12), 3756–3757 (1999)
29. M. Walter, J. Akola, O. Lopez-Acevedo, P.D. Jadzinsky, G. Calero, C.J. Ackerson, R.L. Whetten, H. Grönbeck, H. Häkkinen, A unified view of ligand-protected gold clusters as superatom complexes. *Proc. Natl. Acad. Sci.* **105**, 9157–9162 (2008)
30. O. Lopez-Acevedo, J. Akola, R.L. Whetten, H. Grönbeck, H. Häkkinen, Structure and bonding in the ubiquitous icosahedral metallic gold cluster  $Au_{144}(SR)_{60}$ . *J. Phys. Chem. C* **113**, 5035–5038 (2009)
31. O. Lopez-Acevedo, H. Tsunoyama, T. Tsukuda, H. Häkkinen, C.M. Aikens, Chirality and electronic structure of the thiolate-protected  $Au_{38}$  nanocluster. *J. Am. Chem. Soc.* **132**(23), 8210–8218 (2010)
32. Z. Wang, O. Toikkanen, B.M. Quinn, R.E. Palmer, Real-space observation of prolate monolayer-protected  $Au_{38}$  clusters using aberration-corrected scanning transmission electron microscopy. *Small* **7**(11), 1542–1545 (2011)
33. Z.Y. Li, N.P. Young, M. Di Vece, S. Palomba, R.E. Palmer, A.L. Bleloch, B.C. Curley, R.L. Johnston, J. Jiang, J. Yuan, Three-dimensional atomic-scale structure of size-selected gold nanoclusters. *Nature* **451**(7174), 46–48 (2008)
34. B.C. Curley, R.L. Johnston, N.P. Young, Z.Y. Li, M. Di Vece, R.E. Palmer, A.L. Bleloch, Combining theory and experiment to characterize the atomic structures of surface-deposited  $Au_{309}$  clusters. *J. Phys. Chem. C* **111**(48), 17846–17851 (2007)
35. N.J. Cookson, *Preparation and Characterisation of Bimetallic Core-Shell Nanoparticles*, School of Chemistry, University of Birmingham, Edgbaston, Birmingham, Master's thesis, 2009
36. M.J. Cabrera-Trujillo, J.M. Montejano-Carrizales, J.L. Rodriguez-Lopez, W. Zhang, J.J. Velazquez-Salazar, M. José-Yacamán, Nucleation and growth of stellated gold clusters: experimental synthesis and theoretical study. *J. Phys. Chem. C* **114**(49), 21051–21060 (2010)

37. R.L. Johnston, Evolving better nanoparticles: genetic algorithms for optimising cluster geometries. *Dalton Trans.* **22**, 4193 (2003)
38. F. Pittaway, L.O. Paz-Borbón, R.L. Johnston, H. Arslan, R. Ferrando, C. Mottet, G. Barcaro, A. Fortunelli, Theoretical studies of palladium-gold nanoclusters: Pd-Au clusters with up to 50 atoms. *J. Phys. Chem. C* **113**, 9141–9152 (2009)
39. R. Ismail, R.L. Johnston, Investigation of the structures and chemical ordering of small pd-au clusters as a function of composition and potential parameterisation. *Phys. Chem. Chem. Phys.* **12**(30), 8607–8619 (2010)
40. B. Shan, L. Wang, S. Yang, J. Hyun, N. Kapur, Y. Zhao, J.B. Nicholas, K. Cho, First-principles-based embedded atom method for PdAu nanoparticles. *Phys. Rev. B* **80**, 035404 (2009)
41. H.B. Liu, U. Pal, A. Medina, C. Maldonado, J.A. Ascencio, Structural incoherency and structure reversal in bimetallic Au–Pd nanoclusters. *Phys. Rev. B* **71**, 075403 (2005)
42. A.R. Miedema, Surface energy of solid metals. *Z. Metal.* **69**(5), 287–292 (1978)
43. D. Ferrer, A. Torres-Castro, X. Gao, S. Sepúlveda-Guzmán, U. Ortiz-Méndez, M. José-Yacamán, Three-layer core/shell structure in Au-Pd bimetallic nanoparticles. *Nano Lett.* **7**, 1701–1705 (2007)
44. T.P. Martin, Shells of atoms. *Phys. Rep.* **273**, 199–241 (1996)
45. X. Xing, B. Yoon, U. Landman, J.H. Parks, Structural evolution of Au nanoclusters: From planar to cage to tubular motifs. *Phys. Rev. B* **74**(16), 165423 (2006)
46. A.J. Logsdail, R.L. Johnston, Interdependence of structure and chemical order in high symmetry (pdau)<sub>N</sub> nanoclusters. *RSC Adv.* **2**, 5863–5869 (2012)
47. J.N. Murrell, R.E. Mottram, Potential energy functions for atomic solids. *Mol. Phys.* **69**, 571–585 (1990)
48. A.P. Sutton, J. Chen, Long-range Finnis-Sinclair potentials. *Philos. Mag. Lett.* **61**(3), 139–146 (1990)
49. M.S. Daw, M.I. Baskes, Embedded-atom method: derivation and application to impurities, surfaces, and other defects in metals. *Phys. Rev. B* **29**(12), 6443–6453 (1984)
50. R.P. Gupta, Lattice relaxation at a metal surface. *Phys. Rev. B* **23**(12), 6265–6270 (1981)
51. R. Ferrando. Personal communication, 2009.
52. C. Kittel, *Introduction To Solid State Physics*, 6th edn. (Wiley, New York, 1986)
53. C.L. Cleveland, U. Landman, The energetics and structure of nickel clusters: size dependence. *J. Chem. Phys.* **94**(11), 7376–7396 (1991)
54. J. Uppenbrink, D.J. Wales, Structure and energetics of model metal clusters. *J. Chem. Phys.* **96**(11), 8520–8534 (1992)
55. A.J. Logsdail, Z.Y. Li, R.L. Johnston, Faceting preferences for au<sub>N</sub> and pd<sub>N</sub> nanoclusters with high-symmetry motifs. *Phys. Chem. Chem. Phys.* **15**, 3473 (2013)
56. J. Uppenbrink, R.L. Johnston, J.N. Murrell, Modelling transition metal surfaces with empirical potentials. *Surf. Sci.* **304**(1–2), 223–236 (1994)
57. Nanoalloys: From theory to applications. *Faraday Discussions No.138*, vol. 138, 2008.

Computational Characterisation of Gold Nanocluster  
Structures

Logsdail, A.J.

2013, XVI, 209 p. 99 illus., 84 illus. in color., Hardcover

ISBN: 978-3-319-01492-0